5

Anatomy of the AGN in NGC 5548: IX. Photoionized emission features in the soft X-ray spectra

Junjie Mao, J. S. Kaastra, M. Mehdipour, Liyi Gu, E. Costantini, G. A. Kriss, S. Bianchi, G. Branduardi-Raymont, E. Behar, L. Di Gesu, G. Ponti, P.-O. Petrucci, and J. Ebrero

The X-ray narrow emission line region (NELR) of the archetypal Seyfert 1 galaxy NGC 5548 has been interpreted as a single-phase photoionized plasma that is absorbed by some of the warm absorber components. This scenario requires these overlaying warm absorber components to be at a greater distance (from the central engine) than the X-ray NELR, which is not fully consistent with the distance estimates found in the literature. Therefore, we reanalyze the high-resolution spectra obtained in 2013–2014 with the Reflection Grating Spectrometer (RGS) on board *XMM*-Newton to provide an alternative interpretation of the X-ray narrow emission features. We find that the X-ray narrow emission features in NGC 5548 can be described by a two-phase photoionized plasma with different ionization parameters ($\log \xi = 1.3$ and 0.1) and kinematics ($v_{\rm out} = -50$ and -400 km s^{-1}),

This chapter has been published in Astronomy & Astrophysics, 2018, 612, A18.

but no further absorption by the warm absorber components. The X-ray and optical NELR might be the same multiphase photoionized plasma. The X-ray and the optical NELRs have comparable distances and asymmetric line profiles, and the underlying photoionized plasma is turbulent and compact in size. The X-ray NELR is not the counterpart of the UV/X-ray absorber outside the line of sight because their distances and kinematics are not consistent. In addition, X-ray broad emission features that we find in the spectrum can be accounted for by a third photoionized emission component. The RGS spectrum obtained in 2016 is analyzed as well, where the luminosity of most prominent emission lines (the O VII forbidden line and O VIII Lyα line) are the same (at a 1 σ confidence level) as in 2013–2014.

5.1. Introduction

Two types of emission lines are commonly observed in the optical spectra of active galactic nuclei (AGN): broad emission lines with a velocity broadening of a few 10^3 km s^{-1} and narrow emission lines with a velocity broadening of a few 10^2 km s^{-1}. The optical broad and narrow emission lines stem from the broad and narrow emission line regions (BELR and NELR, see Netzer 2015, for a recent review); the former are closer to the central engine (a few light days to weeks, Peterson et al. 2004) and the latter farther away (at least a few parsecs, Bennert et al. 2006a,b). In the X-ray band, broad and narrow emission lines are also observed (e.g., Costantini et al. 2007, 2016; Kaastra et al. 2000; Steenbrugge et al. 2005), often along with the characteristic narrow radiative recombination continua (RRC) of a photoionized plasma. The spatial extent and overall morphology of the optical and the X-ray NELRs are remarkably similar in a small sample of nearby Seyfert 2 galaxies (Bianchi et al. 2006). Nonetheless, there is no conclusive evidence that the optical and X-ray narrow emission features originate from the same photoionized plasma with a multiphase nature.

In terms of detailed spectral modeling of the narrow emission features in the X-ray band, a two-step approach is commonly used. First, a phenomenological local fit (e.g., Guainazzi & Bianchi 2007) is performed for individual emission lines and RRC. Typically, the (local) continuum is simply modeled as a (local) power law or spline function plus a model for RRC, and an emission line is modeled with a Gaussian or delta profile. The local fit is straightforward and useful, and provides primary information: whether a single line is shifted and/or broadened, the temperature of a photoionized plasma (via the width of the RRC), the temperature and density of the plasma (via the line ratios of the He-like triplets), etc.

With the knowledge obtained from the local fit, the entire spectrum is then modeled with a self-consistent plasma model or with a combination of plasma models (e.g., Guainazzi et al. 2009). The plasma model can be a photoionized plasma either with a single photoionized component (e.g., Whewell et al. 2015) or multiple photoionized components (e.g., Armentrout et al. 2007; Kallman et al. 2014; Kinkhabwala et al. 2002; Longinotti et al. 2008; Marinucci et al. 2011; Nucita et al. 2010), and sometimes a collisional ionized equilibrium (CIE) plasma, which is associated with star formation (Guainazzi et al. 2009) or jets (Bianchi et al. 2010).

For the photoionized plasma model, the widely used approach is to simulate a set of photoionized spectra with the Cloudy code (Ferland et al. 2017) for a fixed ionizing spectral energy distribution (SED) and for a grid of physical parameters, including

the ionization parameter, the line of sight column density, and sometimes the plasma number density and microscopic turbulence velocity as well. The number of free parameters and the size of the grid are limited; otherwise, it is computationally too expensive to simulate. Subsequently, the observed spectra are compared with these pre-calculated models, and the best-fit of the physical parameters is derived from the closest match. This last step is carried out in a separate spectral fitting package, e.g., XSPEC (Arnaud 1996).

A different approach for the photoionized plasma model is used here (see also Mao et al. 2017). We use SPEX (v3.03.02 Kaastra et al. 1996) to fit the entire observed spectra on the fly. The advantage of the SPEX code is that it includes an extensive atomic database and self-consistent plasma models, e.g., PION[1] for the photoionized plasma, which utilizes state-of-the-art atomic data (Kaastra 2017b). We refer to Mehdipour et al. (2016a) for a detailed comparison of the photoionization calculation between SPEX, Cloudy, and XSTAR (Bautista & Kallman 2001; Kallman & Bautista 2001). In each step of the photoionized plasma fitting the intrinsic SED, thermal equilibrium, ionization balance, level population, transmission, emissivity, and line broadening are calculated in real time to account for the absorption and emission features self-consistently. In short, the photoionization calculation is consistent with the instant ionizing SED and without pre-calculations using grid-defined parameters, thus more freedom and higher consistency can be achieved in SPEX.

NGC 5548 is the archetypal Seyfert 1 galaxy, with broad and narrow emission features across its optical to X-ray spectra (e.g., Chiang et al. 2000; Kaastra et al. 2002; Korista et al. 1995; Peterson et al. 2002; Steenbrugge et al. 2005). The extensive multiwavelength campaign of NGC 5548 in 2013–2014 (Kaastra et al. 2014; Mehdipour et al. 2015) unveiled a special state of the source, where the soft X-ray flux is highly obscured. Such a special state offers a unique opportunity to study the narrow emission lines and radiative recombination continua that were previously hidden by the unobscured continuum (Detmers et al. 2009; Kaastra et al. 2002; Steenbrugge et al. 2005). With a detailed study of the narrow emission features using both the local fit and Cloudy based photoionization modeling, Whewell et al. (2015) interpret the X-ray NELR as a single-phase photoionized plasma that is absorbed by the warm absorber components B+E or A+B+C (see Table S2 of Kaastra et al. 2014, for the nomenclature). That is to say, these warm absorber

[1]The model description and a list of parameters for the PION model can be found in the SPEX manual (Section 4.29).

components intervene along the line of sight from the X-ray narrow line emitter to the observer.

This scenario does not fully agree with the distance estimates of the X-ray NELR and warm absorber components in NGC 5548. Using the variability of the forbidden line of O VII, Detmers et al. (2009) derived a distance of 1–15 pc for the X-ray NELR, consistent with the optical NELR distance estimate of 1–3 pc (Peterson et al. 2013) and joint optical and X-ray NELR distance estimate of ~ 2.4 pc (Landt et al. 2015). According to the Cloudy-based photoionization model, Whewell et al. (2015) found that the X-ray narrow emission lines originate mainly from the illuminated face of the X-ray NELR with a distance of 14 pc. Ebrero et al. (2016) estimate the distance of the warm absorber components based on variability, with component A and B at least 10 pc away from the central engine and components C to F within 5 pc from the central engine. Nonetheless, based on a spectral analysis using the density sensitive metastable absorption lines, Mao et al. (2017) find that the warm absorber component B is even closer (< 0.23 pc, 3σ upper limit) than the optical NELR rather than farther away. Ebrero et al. (2016) constrain the lower limit of the distance of the warm absorber component B based on the non-detection of variability on a timescale of 500 days. However, the authors also point out that there are marginal hints of variability at 4 and 60 days. If the variability at a shorter timescale is true, the inferred distance of component B would be much smaller.

Therefore, we reanalyze the high-resolution spectra of NGC 5548 obtained with the Reflection Grating Spectrometer (RGS, den Herder et al. 2001) on board *XMM-Newton* (Jansen et al. 2001) to provide an alternative interpretation of the X-ray narrow emission features. To be more specific, we attempt to model the soft X-ray emission features with a multiphase photoionized plasma with no additional absorption by the warm absorber components. Whewell et al. (2015) did not consider this scenario in their study.

In Section 6.2, we present the observed RGS spectrum. We describe the detailed spectral analysis in Section 6.3, including the phenomenological local fit (Section 5.3.1) and the physical global fit (Section 5.3.2). The physical global fit is based on the self-consistent photoionization model PION in the SPEX code, with both the single-phase and multiphase scenarios studied. We discuss the relation between the X-ray and optical narrow emission line region in Section 5.4.1 and the relation between the X-ray emitter and absorber in Section 5.4.2, respectively. We justify our usage of the unobscured ionizing SED for the X-ray emitter in Section 5.4.3. We also point out the abnormally high Lyγ/Lyα ratio of N VII and discuss it in terms

Table 5.1: Observation log of NGC 5548 in 2016 (PI: G. Kriss) with *XMM*-Newton.

Start date	Exp. (ks)	ObsID
2016-01-14	37	0771000101
2016-01-16	34	0771000201

Notes. The observation log for 2013–2014 can be found in Table 1 in Mehdipour et al. (2015).

of a possible charge exchange component in Section 5.4.4. The summary can be found in Section 6.4.5.

5.2. Observations and data reduction

The RGS data used here were obtained in two epochs, June 2013 – February 2014 (PI: J. Kaastra) and January 2016 (PI: G. Kriss), respectively. Data for the first epoch (2013–2014) were taken as part of a large multiwavelength campaign of NGC 5548 (Kaastra et al. 2014). There are in total 14 XMM-*Newton* observations (∼50 ks exposure each), 12 taken between 22 June and 31 July 2013 and 2 more taken in December 2013 and February 2014. The observation log for 2013–2014 can be found in Mehdipour et al. (2015, their Table 1); our Table 6.1 lists the observation log for 2016.

Details of the RGS data reduction method are similar to those described in Kaastra et al. (2011). The first-order RGS1 and RGS2 spectra for all observations are stacked for each epoch, with a total exposure of ∼770 ks (for 2013–2014) and ∼70 ks (for 2016), respectively. The stacked RGS spectrum of 2013–2014 is the same as that used by Whewell et al. (2015) for the study of the narrow emission features.

5.3. Spectral analysis and results

SPEX v3.03.02 is used for the spectral analysis. We use the C-statistic throughout this work (Kaastra 2017a). Statistical errors are quoted at the 68% confidence level ($\Delta C = 1.0$), unless indicated otherwise. The spectral fit is performed in the 7–35 wavelength range. The stacked 2013–2014 and 2016 spectra are both optimally binned (Kaastra & Bleeker 2016) for the following spectral analysis (Sect. 6.3). The redshift of the AGN is fixed to $z = 0.017175$ (de Vaucouleurs et al. 1991), as given in the NASA/IPAC Extragalactic Database (NED).

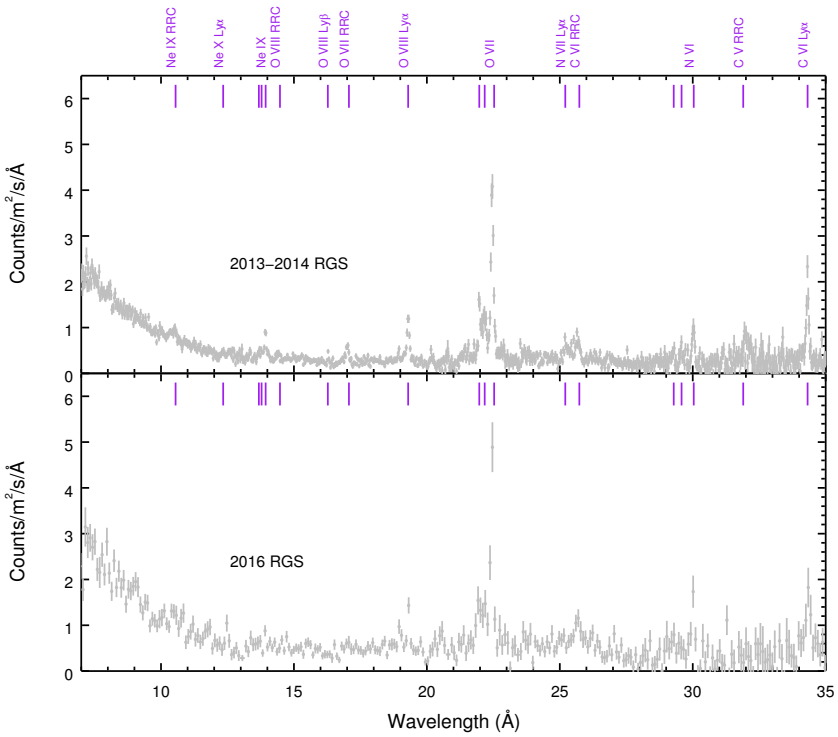

Figure 5.1: Stacked RGS spectra (in the observed frame) in 2013–2014 (upper panel) and 2016 (lower panel, rebinned for clarity).

5.3.1. Phenomenological local fit

In order to check the variability of the narrow emission features between 2013–2014 and 2016, we perform a simple local fit to spectra from the two epochs with a spline continuum model (SPLN in SPEX, see also Detmers et al. 2008), Gaussian line models (GAUS), and radiative recombination continua (RRC).

Even in the 770 ks 2013-2014 spectrum, the X-ray broad emission lines are difficult to fit due to their low significance (Whewell et al. 2015). Therefore, in this exercise, we do not include them in either spectra. In the 2016 spectrum, the Lyα line of O VIII and the forbidden line of O VII can be relatively well constrained, with statistical uncertainties $\lesssim 20\%$. The rest of the lines and RRC given in Table 5.2 have statistical uncertainties between 30% and 100% in the 2016 spectrum. In Table 5.2 we compare the intrinsic (unabsorbed) luminosity of these lines and RRC between the two epochs.

The most prominent narrow emission lines (the O VIII Lyα and O VII forbidden

Table 5.2: Intrinsic (unabsorbed) luminosity of the prominent narrow emission features for the 2013–2014 and 2016 RGS spectra of NGC 5548.

Ion	Line/RRC	λ_0 Å	$L_{2013-2014}$ 10^{32} W	L_{2016} 10^{32} W
Ne IX	$1s^2$	10.37	10.3 ± 5.6	23 ± 22
Ne IX	Heα (f)	13.70	6.7 ± 1.2	3.9 ± 2.2
O VII	$1s^2$	16.79	8.7 ± 1.6	6.4 ± 5.6
O VIII	Lyα	18.97	11.2 ± 0.7	11.2 ± 1.9
O VII	Heα (f)	22.10	35.7 ± 1.8	39.5 ± 5.4
C VI	$1s$	25.30	13.9 ± 6.6	8.9 ± 6.7
N VI	Heα (f)	29.53	6.4 ± 0.9	13.5 ± 4.3
C VI	Lyα	33.74	11.7 ± 1.2	8.3 ± 5.6

Notes. λ_0 is the rest-frame wavelength.

lines) have remained constant (at a 1σ confidence level) in the two epochs June 2013 – February 2014 and January 2016. This is not totally unexpected, as shown in Table 2 of Detmers et al. (2009); the O VII line flux is also consistent within 1σ for two epochs on a similar timescale, December 1999 – February 2000 and January 2002.

On the other hand, some weak features might have varied by a factor of 2 (the Ne IX RRC and N VI forbidden line), but still within a 2σ confidence level.

5.3.2. Physical global fit

For the physical global fit (Section 5.3.2), we first model the high-quality 2013–2014 spectrum with different models (Section 5.3.2.1). Then we simply apply the best-fit model to the low-quality 2016 spectrum (Section 5.3.2.2).

Our global fit includes the following components: (1) the intrinsic broadband spectral energy distribution (SED) of the AGN; (2) the Galactic absorption; (3) the continuum absorption caused by the obscurer; (4) the absorption features caused by the warm absorber; and (5) the narrow and/or broad emission features caused by the X-ray emitter.

The intrinsic SED consists of a Comptonized disk component (COMT in SPEX, for optical to soft X-ray), a power-law component (POW for X-ray), and a reflection component (REFL for the Fe K line and hard X-ray). For the 2013–2014 spectral analysis, all the relevant parameters are fixed to those values given in Mehdipour

et al. (2015), where the best constraints on these parameters have been obtained from multiwavelength data. For the 2016 spectral analysis, we fixed the parameters in the COMT component to values that corresponds to the average UVW2 flux in 2016 (the correlations can be found in Mehdipour et al. 2016b). The power-law and reflection components are allowed to vary in order to match the EPIC-pn data.

The Galactic absorption with $N_{\rm H} = 1.45 \times 10^{24}$ m^{-2} (Wakker et al. 2011) is modeled with the collisional ionization equilibrium absorption model (hereafter HOT) (de Plaa et al. 2004; Steenbrugge et al. 2005) in SPEX. The electron temperature of the HOT component is fixed to 0.5 eV to mimic the transmission of a neutral gas.

The continuum absorption caused by the obscurer is modeled with two XABS components (Kaastra et al. 2014; Mehdipour et al. 2017). The line of sight (LOS) hydrogen column densities ($N_{\rm H}$) and absorption covering factors ($f_{\rm cov}$) are allowed to vary in both 2013–2014 and 2016 spectra. The ionization parameters of the two XABS components are treated differently: the warmer one is allowed to vary ($\log \xi \sim -1$) and the cooler one is fixed to -4 (Di Gesu et al. 2015).

The absorption features caused by the warm absorber are accounted for using six PION components. In both the 2013–2014 and 2016 spectra the hydrogen column densities ($N_{\rm H}$), outflow velocities ($v_{\rm out}$), and microscopic turbulence velocities ($v_{\rm mic}$) of the PION components are fixed to the values given in Mao et al. (2017), which are obtained by fitting the high-quality 2002 *Chandra* grating spectra of NGC 5548. Nonetheless, the ionization parameters ($\log \xi$) can differ for these three epochs, due to the variability of the obscurer and to the changes in the intrinsic SED (Cappi et al. 2016). The ionization parameters are assumed to be proportional to the $1 - 10^3$ Ryd ionizing luminosity. That is to say, the number density times distance squared ($n_{\rm H} r^2$) in the two later epochs is assumed to be the same as in 2002.

The narrow and broad emission features caused by the X-ray emitter (sometimes called the warm mirror) are also modeled with PION. Six free parameters of each emission PION component are allowed to vary, including the hydrogen column densities ($N_{\rm H}$), ionization parameters ($\log \xi$), outflow velocities ($v_{\rm out}$), turbulence velocities ($v_{\rm mic}$), and the emission covering factors ($C_{\rm cov}$, see next paragraph). Additionally, each emission PION component is convolved with a Gaussian velocity broadening model (VGAU in SPEX), with the velocity parameter ($v_{\rm mac}$) free to vary, to account for macroscopic motion.

It should be noted that there are two covering factors in the PION model. The absorption covering factor $f_{\rm cov}$ is used to model any partial covering in the line

of sight (similar to that of the XABS component). The emission covering factor, $C_{\rm cov} = \Omega/4\pi$, corresponds to the normalized solid angle sustained by the emitting region as seen from the central engine. In our modeling, each absorption PION component has fixed $f_{\rm cov} = 1$ and $C_{\rm cov} = 0$, while each emission PION component has fixed $f_{\rm cov} = 0$ and free $C_{\rm cov} \in (0,\ 1)$. Furthermore, the ionizing SED for the absorption PION components is the obscured SED, as the obscurer locates between the warm absorber and the central engine (Kaastra et al. 2014). Nevertheless, the ionizing SED received by the emission PION components is assumed to be unobscured, and we will discuss this in detail in Section 5.4.3. Unless indicated otherwise, the proto-solar abundances of Lodders & Palme (2009) are used for all plasma models (HOT, XABS, and PION).

5.3.2.1. The 2013–2014 RGS spectrum

Five different models are used for the emission features in the RGS band. We start with a single-phase photoionized emitter (denoted Model S0), which can reproduce well some but not all of the observed narrow emission features. In particular, Model S0 fails to match the RRC of O VII (~17 Å) and C VI (~32 Å), the forbidden lines of N VI (~ 30 Å), etc. The fit residuals can be found in the top panels of Figures 5.2 and 5.3. The residuals indicate that either additional absorption is required or the X-ray emitter has at least two emission components.

Following Whewell et al. (2015), we apply absorption caused by the warm absorber components B+E (Model S1) or A+B+C (Model S2) to the single-phase photoionized emitter. As expected, the C-stat is significantly improved for both models (Table 5.3). Model S2 yields parameters that are more consistent with those of Whewell et al. (2015), i.e., a mildly ionized ($\log \xi \sim 1 - 1.5$), blueshifted ($v_{\rm out} \sim -300$ km s^{-1}), turbulent ($v_{\rm mic} \sim 200$ km s^{-1}) plasma with $N_{\rm H} \sim 10^{25-26}$ m^{-2}. The different values of the best-fit parameters and C-stat between the present work and Whewell et al. (2015) are not unexpected. We use here a narrower wavelength range (7–35 Å), ignoring the 5.7–7 Å and 35–38.2 Å wavelength ranges where the noise is relatively large and no strong lines or RRC are expected. Additionally, due to the different atomic database and calculation used by Cloudy and SPEX, fitting the same high-resolution spectra can lead to best-fit parameters that differ by 10–40% (Mehdipour et al. 2016a).

Alternatively, we also try a model with two emission components (Model D) to account for the narrow emission features. The hotter (~ 4.1 eV) component (EM 1) has a higher luminosity ($\sim 1.2 \times 10^{34}$ W in the 7–35 Å band) and a higher ratio of

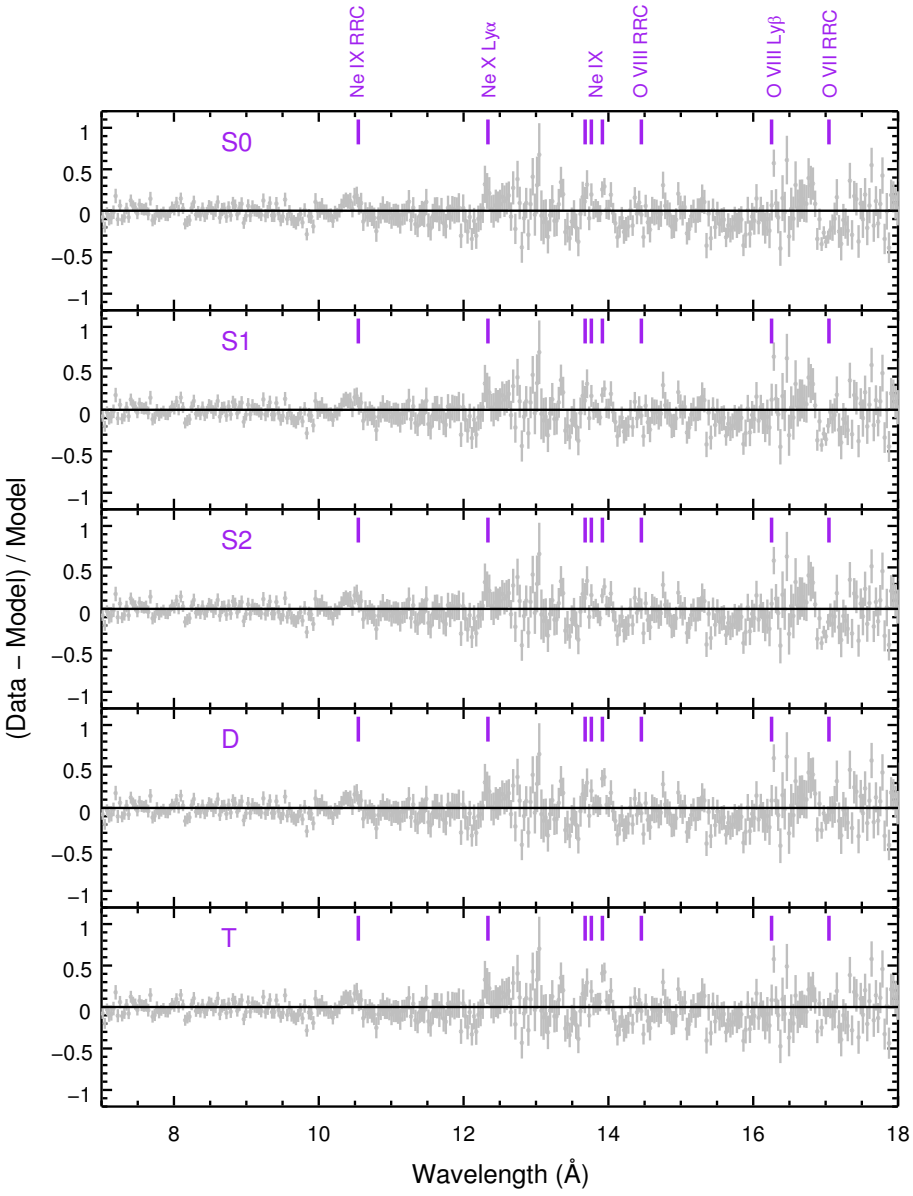

Figure 5.2: Fit residuals of the physical models in the 7–18 Å band.

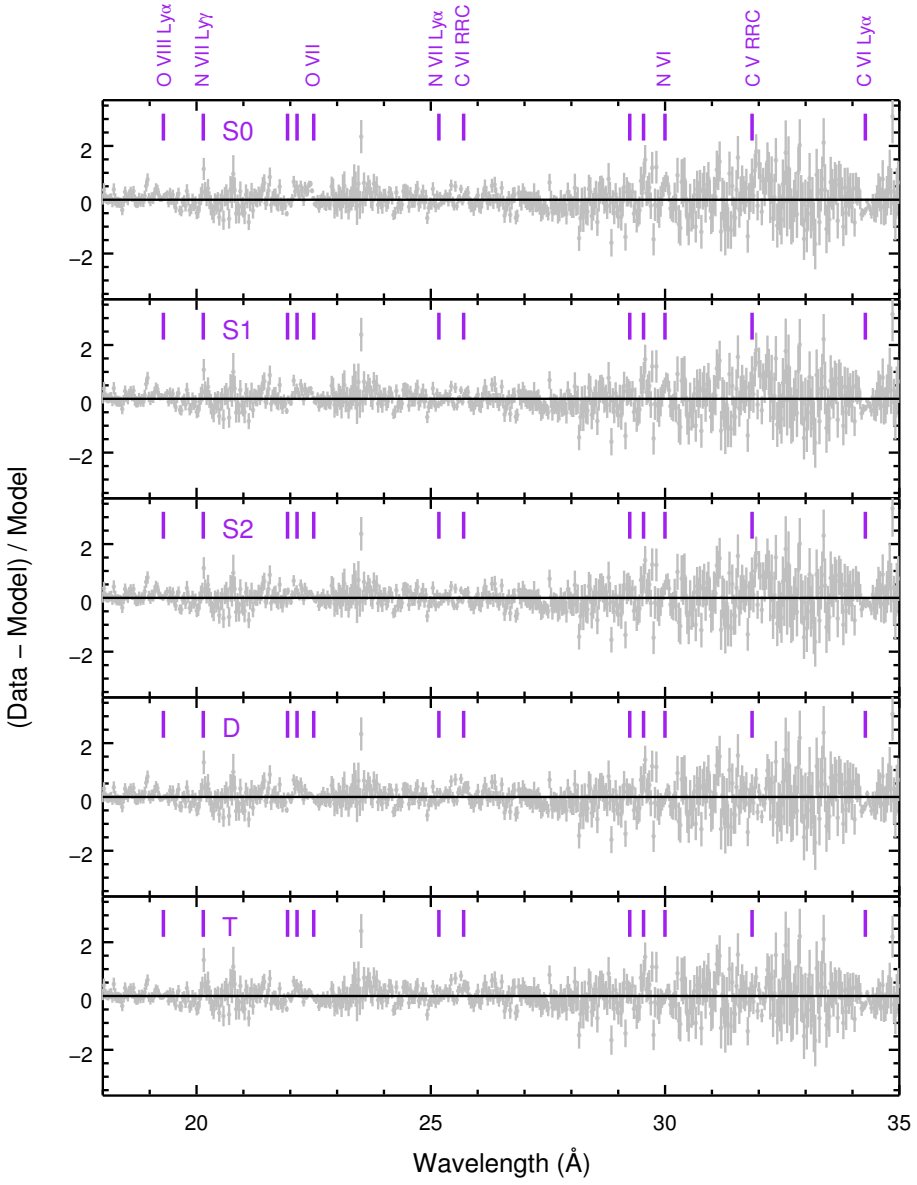

Figure 5.3: As Figure 5.2, but in the 18–35 Å band.

Table 5.3: Photoionized models of the emission features for NGC 5548.

Model	Comp.	$N_{\rm H}$ (10^{25} m^{-2})	log (ξ) (10^{-9} W m)	$v_{\rm mic}$ (km s^{-1})	$v_{\rm out}$ (km s^{-1})	$C_{\rm cov}$ (%)	$v_{\rm mac}$ (km s^{-1})	C-stat	d.o.f.
S0	EM 1	12.7 ± 1.9	1.18 ± 0.02	460 ± 30	-100 ± 20	2.4 ± 0.3	< 210	1774	920
S1	EM 1	12.4 ± 1.4	1.23 ± 0.02	420 ± 30	-190 ± 10	2.9 ± 0.3	< 250	1652	920
S2	EM 1	6.3 ± 1.2	1.20 ± 0.02	200 ± 50	-277 ± 4	6.3 ± 0.9	400 ± 40	1569	920
2*D	EM 1	14.7 ± 0.1	1.30 ± 0.02	520 ± 40	-49 ± 6	1.8 ± 0.6	< 160	2*1567	2*914
	EM 2	19.3 ± 1.3	0.14 ± 0.04	250 ± 60	-410 ± 50	0.60 ± 0.04	< 220		
3*T	EM 1	9.7 ± 1.3	1.31 ± 0.02	400 ± 30	-47 ± 4	2.2 ± 0.2	< 100	3*1525	3*910
	EM 2	30 ± 7	0.13 ± 0.05	< 280	-420 ± 30	0.41 ± 0.07	260 ± 80		
	EM 3	23 ± 6	1.24 ± 0.07	100 (f)	0 (f)	0.5 ± 0.3	7400 ± 1100		

Notes. The emission covering factor ($C_{\rm cov} = \Omega/4\pi$) refers to normalized the solid angle (Ω) subtended with respect to the central engine. The expected C-stat is 935 ± 43 for all the models. The degree of freedom (d.o.f.) is for the RGS band. For EM 3 in Model T, $v_{\rm mic}$ and $v_{\rm out}$ are frozen.

radiation to gas pressure[2] ($\Xi \sim 8$). The cooler (~ 1.6 eV) component (EM 2) has a lower luminosity ($\sim 3.4 \times 10^{33}$ W in the 7–35 Å band) and a lower ratio of radiation to gas pressure ($\Xi \sim 1.4$). The C-stat is improved significantly when comparing Model D to Model S0 ($\Delta C \sim -200$, compared with the root-mean-square deviation 43 of the expected C-stat), but it is negligible ($\Delta C = -2$) when compared to Model S2, as Model D fits the RRC of O VII better, yet the Lyα line of C VI slightly worse. Adding a third emission component (EM 3 in Model T) with a very broad line profile can further improve the C-stat ($\Delta C \sim -40$), but not significantly compared with the root-mean-square deviation 43 of the expected C-stat. The best-fit (Model T) to the 7–35 Å wavelength range RGS data is shown in Figure 5.5.

The narrow emission lines and RRC of Ne X (H-like) and Ne IX (He-like) are underestimated with all the models above. However, adding another emission component with a narrow line profile (including both the turbulent and Gaussian velocity broadening) does not improve the C-stat. An ad hoc solution is to use a super-solar Ne abundance (1.7 ± 0.2) for the highly ionized emission component (EM 1), which fits the Ne emission features well and improves the C-stat ($\Delta C \sim -30$).

In all the models above, the microscopic turbulence velocity ($v_{\rm mic}$) and the macroscopic motion ($v_{\rm mac}$) velocity are highly degenerate. That is to say, the 1σ uncertainties on $v_{\rm mic}$ and $v_{\rm mac}$ are underestimated ($\lesssim 30\%$) when considering either of the two parameters alone, as in Table 5.3. Figure 5.4 shows the confidence level contours of EM 1 and 2 in Model T. In this case, $v_{\rm mac}$ is less well constrained than $v_{\rm mic}$. The former is merely constrained by the velocity broadening of the line, while the latter puts an extra limit on the optical depth of the line. When $v_{\rm mac}$ is negligible, $v_{\rm mic}$ accounts for both the optical depth and velocity broadening. On the other hand, if $v_{\rm mic}$ is negligible (not the case for EM 1 in Model T), $v_{\rm mac}$ dominates the line broadening.

5.3.2.2. The 2016 RGS spectrum

In the global fit of the 2016 spectrum the power-law component, the reflection component, and the two XABS components (Section 5.3.2) are allowed to vary. Assuming the X-ray emitter remains unchanged between the two epochs (Section 5.3.1), with Model T for the narrow and broad emission features the ratio of best-fit C-stat to expected C-stat is 1443/1304 for the RGS band. Contrary to our simple assump-

[2]The ratio of radiation to gas pressure, also known as the pressure form of the ionization parameter, $\Xi = L/(4\pi r^2 n_{\rm H} ckT) = \xi/(4\pi ckT)$, where L is the 1–1000 Ryd ionizing luminosity, r the distance of the slab, $n_{\rm H}$ the hydrogen number density, k the Boltzmann constant, and T the electron temperature (Krolik et al. 1981).

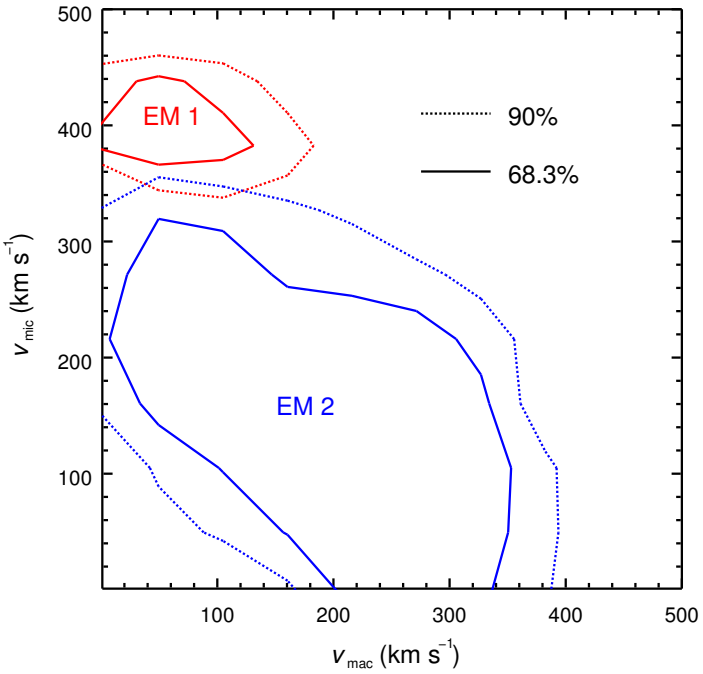

Figure 5.4: Confidence level contours for the microscopic turbulence velocities (v_{mic}) and macroscopic motion velocities (v_{mac}) of EM 1 (in red) and 2 (in blue) in Model T. The solid and dotted contours refer to 68.3% (or $\Delta C = 2.30$) and 90% (or $\Delta C = 4.61$), respectively.

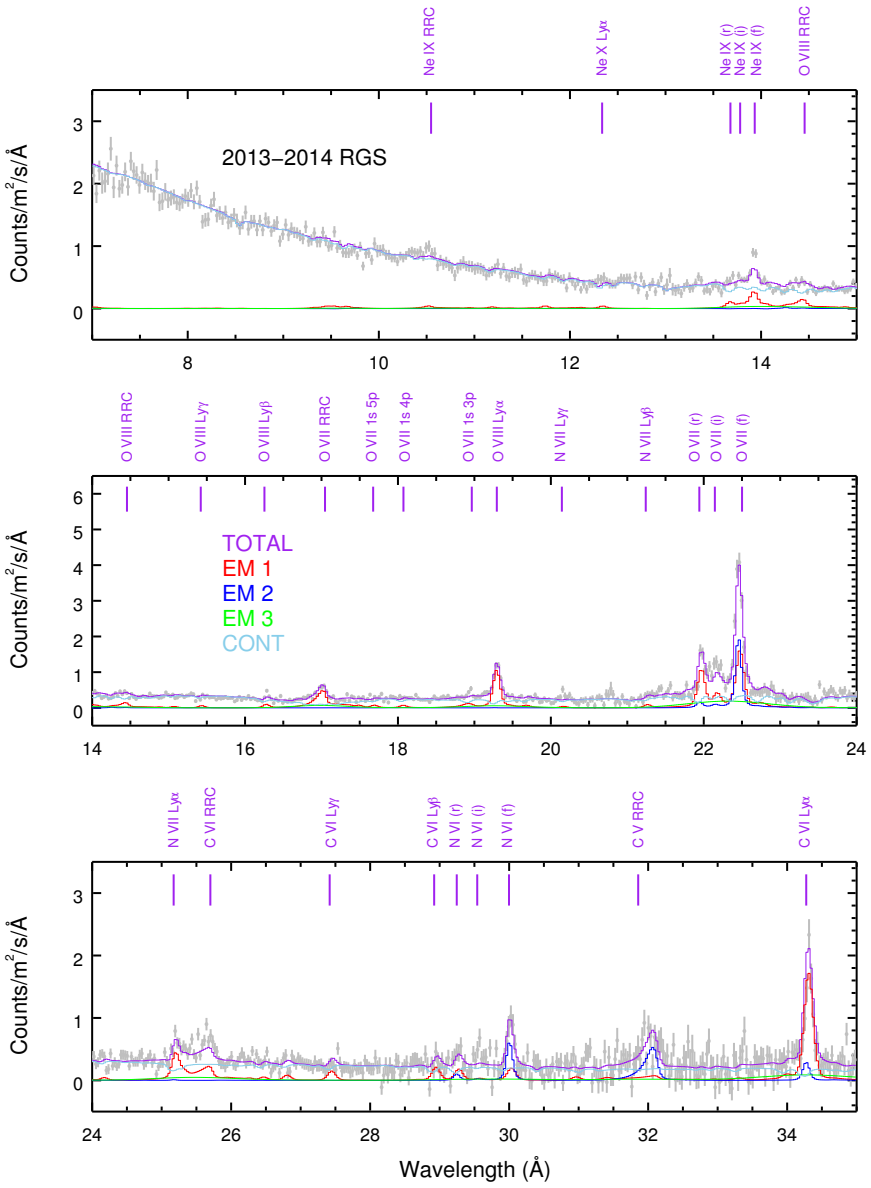

Figure 5.5: Best-fit to the 2013–2014 RGS spectrum with three emission components (Model T) for the narrow and broad emission features.

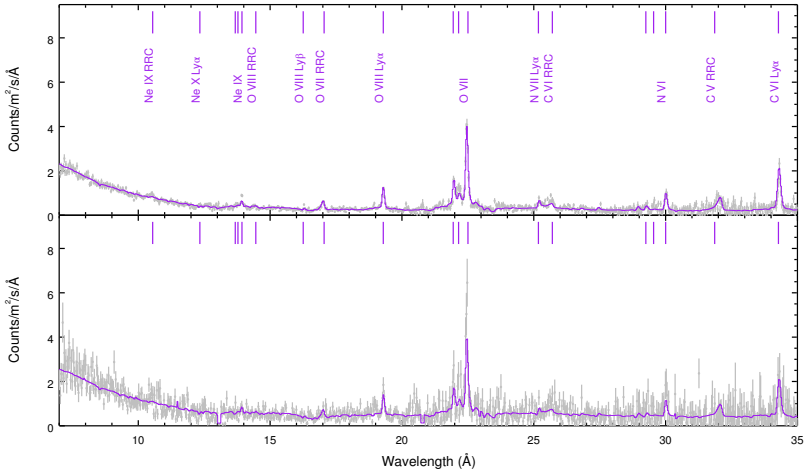

Figure 5.6: With the model of three emission components (Model T), the best-fit to the RGS spectra (in the observed frame) in 2013–2014 (upper panel) and 2016 (lower panel, rebinned for clarity).

tion that the narrow emission features are constant between the two epochs, we find that the forbidden lines of O VII and N VI are underestimated in our model when applied to the 2016 spectrum. These results are similar to what we found with the simple phenomenological fit (Section 5.3.1). Figure 5.6 shows the comparison of the best-fit model to both spectra in 2013–2014 and 2016.

5.4. Discussion

5.4.1. In relation to the optical NELR

From the variability of the optical narrow emission line [O III] 4959 Å and 5007 Å, Peterson et al. (2013) deduced that the optical narrow emission line region (NELR) has a radius of 1–3 pc with $n_{\rm e} \sim 10^{11}$ m^{-3}. A variability study of the X-ray narrow emission line [O VII] 22.10 Å yields an X-ray NELR distance of 1–15 pc (Detmers et al. 2009), which is consistent with the optical NELR. We cannot constrain the density and distance in the X-ray spectra. Although the He-like triplet of O VII is prominent, the associated density diagnostic is not effective since the forbidden-to-intercombination line ratio of O VII is strongly sensitive to the density only when $n_{\rm e} \sim 10^{15-18}$ m^{-3} (Porquet & Dubau 2000, their Fig. 10), which is too high for the NELR.

The asymmetric line profiles of the [O III] lines indicate that the NELR has an

outflowing component, with $\mathrm{HWHM_{blue}/HWHM_{red}} \simeq 2.12$ with an outflow velocity of ~ 460 km s^{-1} (Peterson et al. 2013). Similarly, the line profile of O VII observed in the X-ray band is also asymmetric (see Fig. 3 in Whewell et al. 2015). This can also be seen in our Models D and T, where two emission components with different outflow velocities are required. The emission component (EM 2) that dominates the forbidden lines of O VII and N VI (but not that of Ne IX, see Figure 5.5) is blueshifted (~ -400 km s^{-1}). The other emission component (EM 1), which dominates the Lyα lines of O VIII, N VII and C VI (Figure 5.5), has a negligible outflow velocity. Such divergent kinematic behavior can also be found in the phenomenological fit by Whewell et al. (2015, their Table 6).

We point out that Peterson et al. (2013) attribute the velocity broadening to the virial motion of the gas and no microscopic turbulence velocity broadening is taken into account. As noted by Kraemer et al. (2007), it is possible that microturbulence is present in the optical NELR of NGC 5548. Furthermore, if turbulence dissipates within the NELR, the plasma can be heated in excess of the temperature corresponding to photoionization. In our photoionization modeling of the X-ray narrow emission features, nondissipative microturbulence is taken into account. That is to say, the microscopic and macroscopic velocity broadening are both taken into account, but no extra heating is used to solve the thermal equilibrium.

In reality, it is possible that turbulence dissipates within the NELR; in practice, it is difficult to model the emergent spectrum. On the one hand, the extra heating can be included via the external heating option in the PION model[3] if we know the scale length over which the turbulence dissipates, the plasma mass density, and turbulence velocity of the photoionized plasma (Bottorff & Ferland 2002, their Eq. 1). The dissipation scale length and direction, as well as the mass density, can only be assumed in our analysis. On the other hand, the line broadening might appear to be different for the resonance and forbidden lines. Considering a slab with suitable ionization parameter for the resonance and forbidden lines, assuming that the turbulence dissipation direction is along the line of sight from the central engine toward the observer and that the dissipation length scale equals the size of the slab, the observed broadening of the forbidden lines is the integrated result of velocity broadening across the entire slab because they are optically thin. In contrast, due to the large optical depth, the observed resonance lines are only those escaping from the skin ($\tau \sim 1$) of the far side of the slab (with respect to

[3] In Kraemer et al. (2007), the dissipative heating is introduced via the additional heating terms in the Cloudy modeling.

the central engine); therefore, they are less broadened since turbulence converts to heating at the far side. In short, in order to model the emergent spectrum of a dissipative turbulent photoionized plasma, several assumptions are required, and the line broadening effects for resonance and forbidden lines are not trivial.

The bottom line is that the total velocity broadening of the narrow emission lines is $300 - 500$ km s^{-1} for individual emission components, well in excess of the thermal broadening. Both the microscopic turbulence and macroscopic motions can contribute to the total velocity broadening, but the two velocities are highly degenerate (Figure 5.4).

Furthermore, regardless of the number of emission components we used for the X-ray narrow emission features, the best-fit emission covering factor $C_{\rm cov} = \Omega/4\pi$ is rather small: $\sim 6\%$ for Model S2 and $2 - 3\%$ for the other models. This implies a compact geometry for the X-ray NELR. We caution that the photoionized plasma is assumed to be uniform with the PION model. If the NELR is clumpy, then the true covering factor can be larger. On the other hand, the optical NELR of NGC 5548 is also found to be compact ($C_{\rm cov} \sim 11\%$, Kraemer et al. 1998).

To summarize, in this work, the X-ray narrow emission features show asymmetric line profiles, and the underlying photoionized plasma is turbulent and compact in size. Similar results have been reported in previous optical studies of the NELR (Kraemer et al. 2007, 1998; Peterson et al. 2013). Moreover, distance estimates (from previous studies) of the X-ray and optical NELR indicate that the two regions might be co-located, i.e., a few parsec away from the central engine (Detmers et al. 2009; Landt et al. 2015; Peterson et al. 2013). These similarities further suggest that the X-ray and optical NELR might be the same multiphase photoionized plasma that manifests its emission in different energy bands. This interpretation has actually been established with the radiation pressure confinement (RPC) model (e.g., Stern et al. 2014). Of course, the RPC model is more sophisticated, where the multiphase photoionized plasma has a range of number densities and ionization parameters. We only have two uniform slabs for the X-ray narrow emission features, but we do notice that the ratio of radiation to gas pressure decreases from the highly ionized component EM 1 to the less ionized component EM 2 (Section 5.3.2.1), which agrees with the RPC model.

Interestingly, based on the measurement of the metastable absorption lines (C III 1175 Å and Si III 1298 Å) in the UV band, Arav et al. (2015) determined the number density ($\log n_{\rm e} = 10.8 \pm 0.1$ m^{-3}) and distance (~ 3.5 pc) of the UV absorption component 1, which are also similar to those of the optical NELR.

5.4.2. In relation to the X-ray warm absorber

As can be seen from Table 5.3, the single-phase emission component fully covered by the warm absorber components A+B+C (Whewell et al. 2015, i.e., Model S2 in this work) and the two-phase emission components with no overlying warm absorber components (Model D) yield comparable fit statistics. Nevertheless, the underlying geometries of the two scenarios are rather different.

In the first scenario (Model S2), the warm absorber components (A to C) are located between the X-ray emitter and the observer, with the warm absorber components fully covering the emission component. Given that the X-ray NELR is compact in size (Section 5.4.1), full covering by the warm absorber components is possible, as long as the warm absorber components are located farther away than the emission component. Ebrero et al. (2016) estimate the distances of the warm absorber components via a variability study. The warm absorber components A and B are at least 10 pc away from the central engine, while component C is between 1 and 5 pc (Figure 5.7).

Nevertheless, a distance estimation based on the density sensitive metastable absorption lines found a 3σ upper limit of 0.23 pc for the warm absorber component B (Mao et al. 2017). If this is the case, and assuming the X-ray NELR has a distance of 1–3 pc, the warm absorber component B cannot absorb the NELR. The second scenario (Model D), with no overlying absorption, does not suffer from the logical difficulty if the warm absorber component B is closer than the X-ray NELR.

Distance (and also density) estimation using either timing or spectral analysis is challenging. Timing analyses usually suffer from low cadence and sometimes the signal-to-noise ratio is not high enough to claim a significant change. On the other hand, spectral analyses (in the X-ray band) suffer from low spectral resolution and limited photon collecting area in the relevant energy band with current grating spectrometers. Future studies with either an intensive monitoring program or a spectral analysis with the next generation spectrometers (e.g., *Arcus,* Smith et al. 2016) are required to better constrain the number density and distance of the warm absorber (Kaastra 2017b).

We also compare the parameters of the emission and absorption components. We list the parameters for selected emission and absorption comparison in Table 5.4. The term $n_{\rm H}r^2$ of the X-ray emission component 1, (X-ray) warm absorber component B, and UV absorption component 1 are comparable ($\sim 10^{44}$ m^{-1}). The distances (thus number densities) of EM 1 are consistent with UV 1, but not with X-ray component B (Figure 5.7). The other parameters ($N_{\rm H}$, $v_{\rm out}$, and $v_{\rm mic}$) of

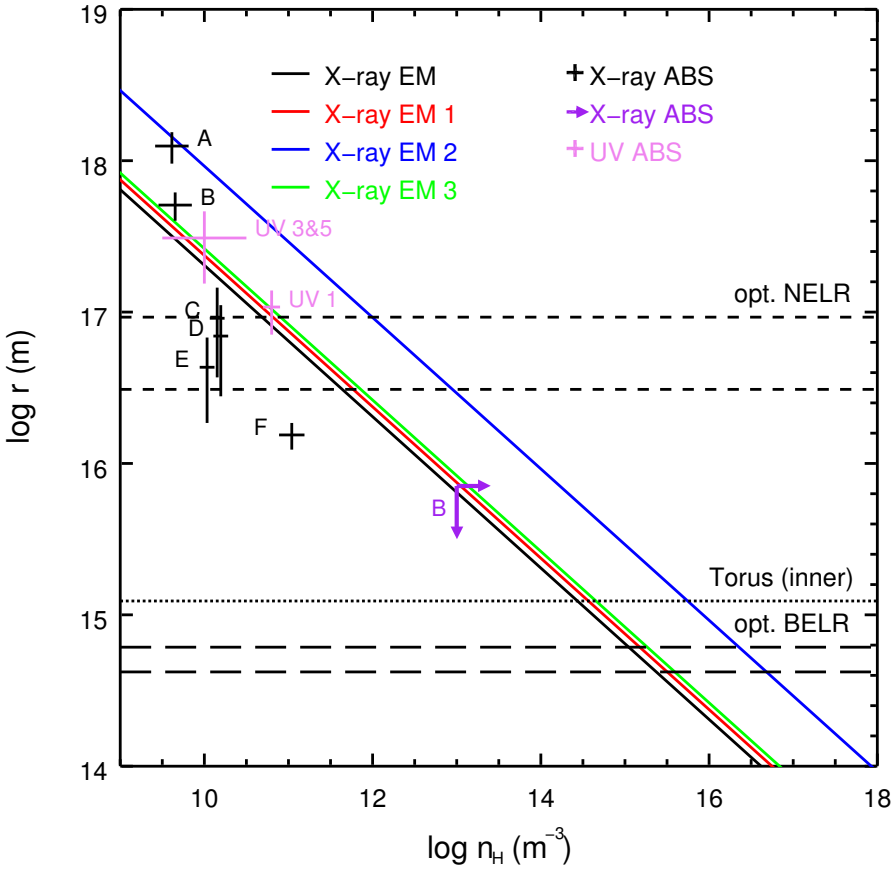

Figure 5.7: Distance and number density of optical, UV, and X-ray emission and/or absorption components in NGC 5548. The solid diagonal lines are the distance and density relations (i.e., $\log \xi = L/n_{\rm H} r^2$) of the X-ray emission components (EM for Whewell et al. 2015, and EM 1–3 for Model T). The black pluses (1σ uncertainties) refer to the six warm absorber components (via a timing analysis, Ebrero et al. 2016). The purple arrows are the 3σ upper (distance) and lower (density) limits of the warm absorber component B (via a spectral analysis, Mao et al. 2017). The pink pluses are for the UV absorption components (Arav et al. 2015). The horizontal short dashed lines refer to the optical narrow emission line region (Peterson et al. 2013). The horizontal long dashed lines refer to the optical broad emission line region (Bottorff et al. 2002; Kaspi et al. 2000). The horizontal dotted line indicates the inner edge of the torus (Suganuma et al. 2006).

these emission and absorption components do not agree with each other. For the X-ray absorption component A and X-ray emission component 2, three parameters ($n_{\rm H}r^2$, o$v_{\rm out}$, and $v_{\rm mic}$) are roughly of the same order of magnitude, but the hydrogen column density and distance (thus number density) are not consistent with each other.

The warm absorber components C to E have similar distances to the X-ray NELR (Figure 5.7), but the inferred number densities are lower by an order of magnitude, while component F has smaller distance and number density than the X-ray NELR (Ebrero et al. 2016). The UV absorption components 3 and 5 are slightly farther away (5–15 pc) than the X-ray NELR, while the distances of components 2, 4, and 6 are not well constrained (Arav et al. 2015).

In short, the emission components are not the counterparts of the UV/X-ray absorption components outside the line of sight.

5

5.4.3. Unobscured SED for the X-ray emitter

Although we have witnessed significant spectral changes since June 2011[4] (Kaastra et al. 2014), we argue that using the unobscured SED for the X-ray emitter (as in Whewell et al. 2015) is reasonable given the following effects.

First, there is a geometric effect. A possible geometry is shown in Fig. 4 of Kaastra et al. (2014) where the obscurer appears along our line of sight, yet only a small part is between the narrow line region and the black hole and the accretion disk.

Second, there is a time delay effect. It is also possible that the X-ray emitter has not yet responded to the changes in the ionizing SED, whether it is obscured or not. The delay timescale ($\tau_{\rm delay}$) is the sum of the light travel time ($\tau_{\rm lt}$) and the recombination time ($\tau_{\rm rec}$). The recombination timescale mainly depends on the number density ($n_{\rm H}$) of the plasma (Krolik & Kriss 1995; Nicastro et al. 1999): the higher the plasma density, the shorter the recombination time. In our photoionization modeling, the recombination timescale for O VII is roughly on the order of $10^{16}\ (n_{\rm H}/{\rm m}^{-3})^{-1}$ s. The light travel time is simply $3.26\ (r_{\rm X}/{\rm pc})$ yr, i.e., $10^8\ (r_{\rm X}/{\rm pc})$ s, where $r_{\rm X}$ is the distance of the X-ray NELR. As long as the number density of the photoionized plasma is $\gtrsim 10^{10}$ m^{-3} and the distance of the X-ray NELR $\gtrsim 1$ pc, the delay time ($\gtrsim$3.3 yr) is longer than the time separation ($\sim$2.6 yr) between our two epochs (2013–2014 and 2016).

[4]There were no observations of NGC 5548 between August 2007 and June 2012 with *XMM*–Newton, *Chandra*, *Suzaku*, or *Swift*.

Table 5.4: Comparing the parameters of selected emission and absorption components.

Comp.	$N_{\rm H}$ (10^{25} m^{-2})	$n_{\rm H} r^2$ (10^{44} m^{-1})	$v_{\rm mic}$ (km s^{-1})	$v_{\rm out}$ (km s^{-1})	E.M. (10^{70} m^{-3})	r (pc)
EM 1	9.7 ± 1.3	5.7 ± 0.3	400 ± 30	-47 ± 4	1.8 ± 0.6	1–3‡
B	0.69 ± 0.09	5.2 ± 0.8	49 ± 14	-550 ± 40	—	< 0.23 or 13–20†
UV 1	$3.2^{+4.7}_{-1.2}$	$7.4^{+4.3}_{-4.5}$	—	-1160	—	$3.5^{+1.0}_{-1.2}$
EM 2	30 ± 7	87 ± 11	< 280	-420 ± 30	16 ± 10	1–3‡
A	0.26 ± 0.08	36 ± 12	150 ± 30	-570 ± 40	—	31–50†

Notes. Results from this work and Peterson et al. (2013, ‡) are used for the narrow emission components (EM 1 and 2 in Model T). The warm absorber components (A and B) are from Mao et al. (2017) and Ebrero et al. (2016, †). The UV absorption component 1 is from Arav et al. (2015). We do not compare the ionization parameter because it can vary, due to the change in the ionizing luminosity. The emission measure (E.M.) is calculated via $n_{\rm e}\ n_{\rm H}\ 4\pi C_{\rm cov} r^2\ N_{\rm H}/n_{\rm H}$.

Third, there is a low-density effect. When the density of the photoionized plasma is sufficiently low, the recombination timescale ($\tau_{\rm rec}$) is orders of magnitude higher than the variability timescale ($\tau_{\rm var}$), and the plasma is in a quasi-steady state. In other words, the ionization balance of the plasma varies slightly around the mean value corresponding to the mean ionizing flux level over time (Kaastra et al. 2012; Nicastro et al. 1999; Silva et al. 2016).

5.4.4. Charge exchange component?

In our physical global fit (Section 5.3.2) to the stacked RGS spectrum in 2013–2014, we find that the N VII Lyγ[5] narrow emission line is abnormally high for a photoionized plasma (all panels in Figure 5.3). When we include a Gaussian profile for the N VII Lyγ narrow emission line, the C-stat is significantly improved with $\Delta C = -23$ at the price of two degrees of freedom. The best-fit line luminosity is $(1.9 \pm 0.5) \times 10^{32}$ W, and the N VII ratio of Lyγ to Lyα is $0.7^{+1.3}_{-0.3}$. Such a high Lyγ/Lyα cannot be explained by a photoionized plasma or a collisionally ionized plasma, but it can be obtained with a charge exchange plasma (e.g., Gu et al. 2015).

It is possible for charge exchange events to occur if a warm ($T \sim 10^{5-6}$ K) outflow runs into the cold ($T \lesssim 1800$ K) torus region. Assuming a constant radial velocity of ~ 300 km s^{-1}, if the outflow is short-lived ($\lesssim 10^{2-3}$ yr), only gas arising beyond the broad line region can reach the torus region (Blustin et al. 2005). If the outflow is long-lived, then outflows arising from the accretion disk can also reach the torus region (Proga 2000). In fact, putative charge exchange emission features at 1223.6 Å, 1242.4 Å, and 1244.0 Å (for Ne X and S XV) in the UV spectrum of NGC 1275 have been reported in Gu et al. (2017).

In our case, using a charge exchange component (the CX model in SPEX, Gu et al. 2016), we can reproduce a N VII Lyγ/Lyα of ~0.7, but the same CX plasma would also produce a high Lyγ/Lyα for C VI and Lyδ/Lyα for O VIII (~0.5), which are not found in the observed spectra. Therefore, we are not convinced that the N VII Lyγ/Lyα ratio alone can validate the presence of a charge exchange plasma in NGC 5548.

5.5. Summary

We reanalyze the high-resolution spectrum of the archetypal Seyfert 1 galaxy NGC 5548 obtained with the Reflection Grating Spectrometer on board *XMM*-Newton in 2013–

[5] 19.83 Å in the rest frame and 20.16 Å in the observed frame.

2014 (770 ks), and analyze the spectrum obtained in 2016 (70 ks). The main results are summarized as follows.

1. The most prominent emission lines (the O VII forbidden line and O VIII Lyα line) are consistent (at a 1 σ confidence level) between 2013–2014 and 2016. This is not totally unexpected, as the nonvariability at such a timescale has been reported previously.

2. The X-ray narrow emission line region (NELR) can be modeled as a two-phase photoionized plasma without further absorption by the warm absorber. This is an alternative to the previous interpretation of the NELR as a single-phase photoionized plasma absorbed by some of the warm absorber components.

3. The X-ray broad emission features can be modeled by a third photoionized component.

4. Our X-ray spectral analysis found that the line profiles of the narrow emission lines are asymmetric, the photoionized plasma is turbulent, and the emission region is compact in size. Similar results have been found in the optical studies. Furthermore, distance estimates from the literature of the X-ray and optical narrow emission line regions suggest that they might be co-located. Therefore, it is possible that the multiphase nature of the NELR manifests its emission in different energy bands.

5. Future missions like *Arcus* are needed in order to better constrain the distances of the warm absorber components. Hence, we can tell whether the warm absorber intervenes along the line of sight from the X-ray narrow line emitter to the observer.

6. The X-ray NELR is not the counterpart of the UV/X-ray absorber outside the line of sight.

7. The N VII Lyγ-to-Lyα ratio is abnormally high in the stacked RGS spectra in 2013–2014. We investigate the possibility that this line may be produced by charge exchange.

References

Arav, N., Chamberlain, C., Kriss, G. A., et al. 2015, A&A, 577, A37
Armentrout, B. K., Kraemer, S. B., & Turner, T. J. 2007, ApJ, 665, 237

Arnaud, K. A. 1996, in Astronomical Society of the Pacific Conference Series, Vol. 101, Astronomical Data Analysis Software and Systems V, ed. G. H. Jacoby & J. Barnes, 17
Bautista, M. A. & Kallman, T. R. 2001, ApJS, 134, 139
Bennert, N., Jungwiert, B., Komossa, S., Haas, M., & Chini, R. 2006a, A&A, 459, 55
Bennert, N., Jungwiert, B., Komossa, S., Haas, M., & Chini, R. 2006b, A&A, 456, 953
Bianchi, S., Chiaberge, M., Evans, D. A., et al. 2010, MNRAS, 405, 553
Bianchi, S., Guainazzi, M., & Chiaberge, M. 2006, A&A, 448, 499
Blustin, A. J., Page, M. J., Fuerst, S. V., Branduardi-Raymont, G., & Ashton, C. E. 2005, A&A, 431, 111
Bottorff, M. & Ferland, G. 2002, ApJ, 568, 581
Bottorff, M. C., Baldwin, J. A., Ferland, G. J., Ferguson, J. W., & Korista, K. T. 2002, ApJ, 581, 932
Cappi, M., De Marco, B., Ponti, G., et al. 2016, A&A, 592, A27
Chiang, J., Reynolds, C. S., Blaes, O. M., et al. 2000, ApJ, 528, 292
Costantini, E., Kaastra, J. S., Arav, N., et al. 2007, A&A, 461, 121
Costantini, E., Kriss, G., Kaastra, J. S., et al. 2016, A&A, 595, A106
de Plaa, J., Kaastra, J. S., Tamura, T., et al. 2004, A&A, 423, 49
de Vaucouleurs, G., de Vaucouleurs, A., Corwin, Jr., H. G., et al. 1991, Third Reference Catalogue of Bright Galaxies. Volume I: Explanations and references. Volume II: Data for galaxies between 0^h and 12^h. Volume III: Data for galaxies between 12^h and 24^h.
den Herder, J. W., Brinkman, A. C., Kahn, S. M., et al. 2001, A&A, 365, L7
Detmers, R. G., Kaastra, J. S., Costantini, E., McHardy, I. M., & Verbunt, F. 2008, A&A, 488, 67
Detmers, R. G., Kaastra, J. S., & McHardy, I. M. 2009, A&A, 504, 409
Di Gesu, L., Costantini, E., Ebrero, J., et al. 2015, A&A, 579, A42
Ebrero, J., Kaastra, J. S., Kriss, G. A., et al. 2016, A&A, 587, A129
Ferland, G. J., Chatzikos, M., Guzmán, F., et al. 2017, , 53, 385
Gu, L., Kaastra, J., & Raassen, A. J. J. 2016, A&A, 588, A52
Gu, L., Kaastra, J., Raassen, A. J. J., et al. 2015, A&A, 584, L11
Gu, L., Mao, J., O'Dea, C. P., et al. 2017, A&A, 601, A45
Guainazzi, M. & Bianchi, S. 2007, MNRAS, 374, 1290
Guainazzi, M., Risaliti, G., Nucita, A., et al. 2009, A&A, 505, 589
Jansen, F., Lumb, D., Altieri, B., et al. 2001, A&A, 365, L1
Kaastra, J. S. 2017a, Astronomische Nachrichten, 338, 146
Kaastra, J. S. 2017b, A&A, 605, A51
Kaastra, J. S. & Bleeker, J. A. M. 2016, A&A, 587, A151
Kaastra, J. S., de Vries, C. P., Steenbrugge, K. C., et al. 2011, A&A, 534, A37
Kaastra, J. S., Detmers, R. G., Mehdipour, M., et al. 2012, A&A, 539, A117
Kaastra, J. S., Kriss, G. A., Cappi, M., et al. 2014, Science, 345, 64
Kaastra, J. S., Mewe, R., Liedahl, D. A., Komossa, S., & Brinkman, A. C. 2000, A&A, 354, L83
Kaastra, J. S., Mewe, R., & Nieuwenhuijzen, H. 1996, in UV and X-ray Spectroscopy of Astrophysical and Laboratory Plasmas, ed. K. Yamashita & T. Watanabe, 411–414
Kaastra, J. S., Steenbrugge, K. C., Raassen, A. J. J., et al. 2002, A&A, 386, 427
Kallman, T. & Bautista, M. 2001, ApJS, 133, 221
Kallman, T., Evans, D. A., Marshall, H., et al. 2014, ApJ, 780, 121
Kaspi, S., Smith, P. S., Netzer, H., et al. 2000, ApJ, 533, 631
Kinkhabwala, A., Sako, M., Behar, E., et al. 2002, ApJ, 575, 732

Korista, K. T., Alloin, D., Barr, P., et al. 1995, ApJS, 97, 285
Kraemer, S. B., Bottorff, M. C., & Crenshaw, D. M. 2007, ApJ, 668, 730
Kraemer, S. B., Crenshaw, D. M., Filippenko, A. V., & Peterson, B. M. 1998, ApJ, 499, 719
Krolik, J. H. & Kriss, G. A. 1995, ApJ, 447, 512
Krolik, J. H., McKee, C. F., & Tarter, C. B. 1981, ApJ, 249, 422
Landt, H., Ward, M. J., Steenbrugge, K. C., & Ferland, G. J. 2015, MNRAS, 454, 3688
Lodders, K. & Palme, H. 2009, Meteoritics and Planetary Science Supplement, 72, 5154
Longinotti, A. L., Nucita, A., Santos-Lleo, M., & Guainazzi, M. 2008, A&A, 484, 311
Mao, J., Kaastra, J. S., Mehdipour, M., et al. 2017, A&A, 607, A100
Marinucci, A., Bianchi, S., Matt, G., et al. 2011, A&A, 526, A36
Mehdipour, M., Kaastra, J. S., & Kallman, T. 2016a, A&A, 596, A65
Mehdipour, M., Kaastra, J. S., Kriss, G. A., et al. 2017, A&A, 607, A28
Mehdipour, M., Kaastra, J. S., Kriss, G. A., et al. 2016b, A&A, 588, A139
Mehdipour, M., Kaastra, J. S., Kriss, G. A., et al. 2015, A&A, 575, A22
Netzer, H. 2015, ARA&A, 53, 365
Nicastro, F., Fiore, F., Perola, G. C., & Elvis, M. 1999, ApJ, 512, 184
Nucita, A. A., Guainazzi, M., Longinotti, A. L., et al. 2010, A&A, 515, A47
Peterson, B. M., Berlind, P., Bertram, R., et al. 2002, ApJ, 581, 197
Peterson, B. M., Denney, K. D., De Rosa, G., et al. 2013, ApJ, 779, 109
Peterson, B. M., Ferrarese, L., Gilbert, K. M., et al. 2004, ApJ, 613, 682
Porquet, D. & Dubau, J. 2000, A&AS, 143, 495
Proga, D. 2000, ApJ, 538, 684
Silva, C. V., Uttley, P., & Costantini, E. 2016, A&A, 596, A79
Smith, R. K., Abraham, M. H., Allured, R., et al. 2016, in Proc. SPIE, Vol. 9905, Space Telescopes and Instrumentation 2016: Ultraviolet to Gamma Ray, 99054M
Steenbrugge, K. C., Kaastra, J. S., Crenshaw, D. M., et al. 2005, A&A, 434, 569
Stern, J., Laor, A., & Baskin, A. 2014, MNRAS, 438, 901
Suganuma, M., Yoshii, Y., Kobayashi, Y., et al. 2006, ApJ, 639, 46
Wakker, B. P., Lockman, F. J., & Brown, J. M. 2011, ApJ, 728, 159
Whewell, M., Branduardi-Raymont, G., Kaastra, J. S., et al. 2015, A&A, 581, A79